JACS
JOURNAL OF THE AMERICAN CHEMICAL SOCIETY
Article
pubs.acs.org/JACS

Engineering Catalytic Contacts and Thermal Stability: Gold/Iron Oxide Binary Nanocrystal Superlattices for CO Oxidation

Yijin Kang,[†] Xingchen Ye,[†] Jun Chen,[‡] Liang Qi,[§] Rosa E. Diaz,[⊥] Vicky Doan-Nguyen,[‡] Guozhong Xing,[‡] Cherie R. Kagan,[†,‡,○] Ju Li,[§,∥] Raymond J. Gorte,[‡,#] Eric A. Stach,[⊥] and Christopher B. Murray*[,†,‡]

[†]Department of Chemistry, University of Pennsylvania, Philadelphia, Pennsylvania 19104, United States
[‡]Department of Materials Science and Engineering, University of Pennsylvania, Philadelphia, Pennsylvania 19104, United States
[§]Department of Nuclear Science and Engineering, MIT, Cambridge, Massachusetts 02139, United States
[∥]Department of Materials Science and Engineering, MIT, Cambridge, Massachusetts 02139, United States
[⊥]Center for Functional Nanomaterials, Brookhaven National Laboratory, Upton, New York 11973, United States
[○]Department of Electrical and Systems Engineering, University of Pennsylvania, Philadelphia, Pennsylvania 19104, United States
[#]Department of Chemical and Biomolecular Engineering, University of Pennsylvania, Philadelphia, Pennsylvania 19104, United States

Supporting Information

ABSTRACT: Well-defined surface, such as surface of a single crystal, is being used to provide precise interpretation of catalytic processes, while the nanoparticulate model catalyst more closely represents the real catalysts that are used in industrial processes. Nanocrystal superlattice, which combines the chemical and physical properties of different materials in a single crystalline structure, is an ideal model catalyst, that bridge between conventional models and real catalysts. We identify the active sites for carbon monoxide (CO) oxidation on Au-FeO_x catalysts by using Au-FeO_x binary superlattices correlating the activity to the number density of catalytic contacts between Au and FeO_x. Moreover, using nanocrystal superlattices, we propose a general strategy of keeping active metals spatially confined to enhance the stability of metal catalysts. With a great range of nanocrystal superlattice structures and compositions, we establish that nanocrystal superlattices are useful model materials through which to explore, understand, and improve catalytic processes bridging the gap between traditional single crystal and supported catalyst studies.

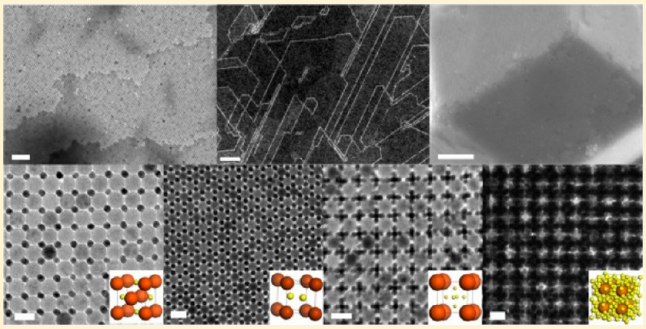

INTRODUCTION

Well-defined surfaces of oriented single crystals have been used for decades to understand the fundamental physical and chemical processes and these insights have been extrapolated to explain the real heterogeneous catalysts which are generally nanoparticles dispersed on a high surface area support.[1,2] The single crystal experiments are usually performed in an ultra-high vacuum (UHV) environment and under controlled conditions, as this allows more precise identification of specific mechanisms that can be obtained from a heterogeneous nanoparticulate system. However, the knowledge gained from single crystal models is not always directly applicable to real catalysts, where distributions in particle size, morphology, surface states and variation in the contacts between catalyst particles or between catalyst particles and the support are all influential.[3] Although challenging, the preparation of well-controlled nanomaterials to bridge conventional models and real catalysts is a focus of intense research.[4−16] Saltsburg, et al. first fabricated a layered synthetic microstructure as model catalyst to isolate the support effects or the nonequilibrium surface structures from the size effects, in the study of catalysis.[17,18] Similarly, Somorjai, et al. have used electron beam lithography to fabricate Pt nanoparticle arrays as model catalysts, allowing control the metal catalyst surface structure, the oxide−metal interface area, and the interparticle distances.[19,20] Moreover, Yang, et al. have reported that a multicomponent nanocrystal (NC) architecture may operate as a tandem catalyst, displaying catalytic properties that are not observed in a simple mixture of the same components.[21]

Recent development in self-assembly allows large-scale fabrication of multicomponent superlattices,[22] which combine the chemical and physical properties of different materials in a periodic architecture (colloidal crystal). This provides a unique opportunity to exploit synergistic interactions and collective properties that arise as NCs couple in these more complex systems.[22−28] In particular, the self-assembly of two types of NC into binary superlattices (BNSLs) is of great interest for the

Received: October 22, 2012
Published: January 7, 2013

   dx.doi.org/10.1021/ja310427u | J. Am. Chem. Soc. 2013, 135, 1499−1505

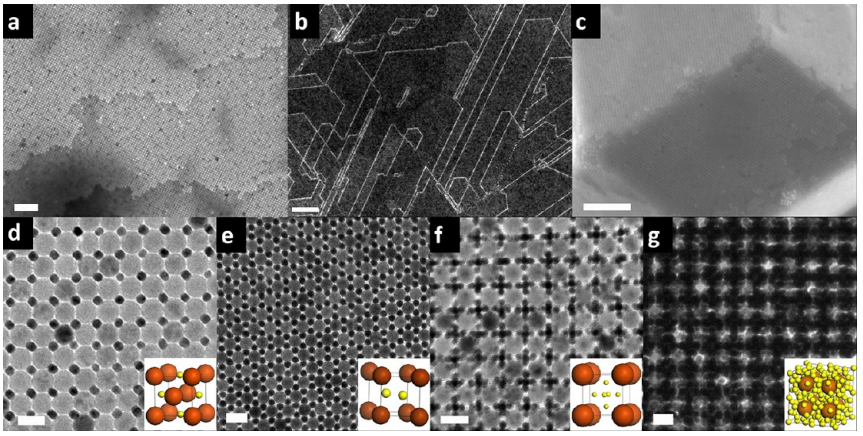

Figure 1. NC superlattices showing characters analogous to single crystals, and the diversified structures. (a) SEM image of Pt−Pd BNSL that has terraces, steps, kinks, and vacancies, similar to those in single crystals. (b) TEM image of Au-FeO_x BNSL that shows grain boundaries. (c) SEM image showing a supercrystal of Pt that has faceted surface. TEM images of Au-FeO_x BNSLs with structures analogous to (d) CuAu, (e) AlB_2, (f) CaB_6, (g) $NaZn_{13}$. Scale bars: (a−c) 200 nm, (d−g) 20 nm.

design of functional metamaterials. With their highly ordered structures and precisely controlled stoichiometry, BNSLs are ideal model for investigating catalytic processes, providing a unique approach to link information gained from the single crystal to supported particulate catalysts. As shown in Figure 1a−c, NC superlattices possess many characteristics of single crystals. Figure 1a exhibits a superlattice showing well-defined terraces, steps, kinks and vacancies. Figure 1b shows that a NC superlattice can have grain boundaries, common in many metal and alloy crystals. Faceted colloidal crystal planes, a characteristic of single crystals, are also observed in NC superlattices (as shown in Figure 1c). Additionally, the NC superlattices can be directed to form a variety of crystal structures by adjusting the relative size and concentration of the constituent NCs. For instance, in the Au-FeO_x (here, FeO_x is A, Au is B) system, AB (Figure 1d), AB_2 (Figure 1e), AB_6 (Figure 1f), and AB_{13} (Figure 1g) structures—analogous to the atomic crystals of CuAu, AlB_2, CaB_6, and $NaZn_{13}$, respectively—are all accessible. Additionally, it is possible to create an A_2B_3 as a thin film, a crystal structure that does not have an atomic counterpart.[29,30] In this work, we exploit the ability to precisely control particle size, relative composition and the character and density of inteparticle contacts to directly correlate BNSL structure with catalytic activity. The classic reaction of CO oxidation on Au provides an ideal model system to demonstrate the benefits of the BNSLs in catalytic studies.

EXPERIMENTAL SECTION

NC Synthesis. We synthesize monodisperse NCs following methods in the literature.[30−35] As-synthesized NCs are purified by size selective precipitation and are redispersed in hexane to form stable solutions with concentrations of 1−10 mg/mL.

Fabrication of NC Superlattice. We fabricate NC superlattice by the liquid−air interface self-assembly method, as described previously.[22,25] The superlattice films are transferred to a Si wafer for catalytic testing, or to a TEM grid for characterization.

Structural and Chemical Characterizations. TEM images are taken on a JEOL1400 TEM at 120 kV. SEM images are taken on JEOL JSM7600F. The HAADF-STEM images and EDX maps are taken using a Hitachi HD2700C 200 kV cold field emission dedicated STEM. Quantitative elemental analyses for the mass of each element in the catalyst film are carried out by dissolving the film with aqua regia, and analysis is performed by inductively coupled plasma optical emission spectrometry (ICP-OES) using a SPECTRO GENESIS ICP spectrometer.

Catalytic Property Measurements. Si wafers covered with superlattice films are loaded in a closed vessel (volume of 40 mL) as a batch reactor. Before the catalytic property measurements, the catalysts are pretreated in pure O_2 at 180 °C for 30 min to remove the organic ligands used in the synthesis procedure (Figure S17). The reactor is evacuated and refilled with 2.5% CO, 50% O_2 and 47.5% He at 150 °C. Aliquots are taken by syringe and injected into a GC equipped with a thermal conductivity detector (TCD). Details are provided in Supporting Information.

Improved Injection-Mode GC Measurements. If a is the initial amount of CO, $n(CO)$ and $n(CO_2)$ are the amount of CO and CO_2 in the reactor, k is the reaction rate, and y is the sampling dose (the amount of sample injected into GC), then at any given reaction time t,

$$2CO + O_2 \rightarrow 2CO_2$$

$$n(CO) = a - kt$$

$$n(CO_2) = kt$$

In a conventional injection-mode measurement, the reading from GC is dependent on the sampling dose y,

$$n(CO)_{GC} = (a - kt)y$$

$$n(CO_2)_{GC} = kty$$

The error of conventional injection-mode measurements is primarily from the inconsistency of each injection (i.e., discrepancy of y).

In an improved measurement, the impact of y can be removed by using the ratio of $[CO]:[CO_2]$, r.

$$r = \frac{n(CO)_{GC}}{n(CO_2)_{GC}} = \frac{(a - kt)y}{kty} = \frac{a - kt}{kt}$$

$$k = \frac{a}{tr + t}$$

The example is given in Supporting Information, Table S2 and Figure S1. Our improved method shows better tolerance to the random error compared to the conventional method. This advantage is especially significant in case that the measurements have limited data points. Theoretically, one single data point collected at any time during the reaction can give the reaction rate, k.

Evaluation of Thermal Stabilities. The superlattice films are transferred to silicon monoxide films covered TEM grids, and are then heated under N_2 atmosphere to evaluate the thermal stabilities. The

dx.doi.org/10.1021/ja310427u | J. Am. Chem. Soc. 2013, 135, 1499−1505

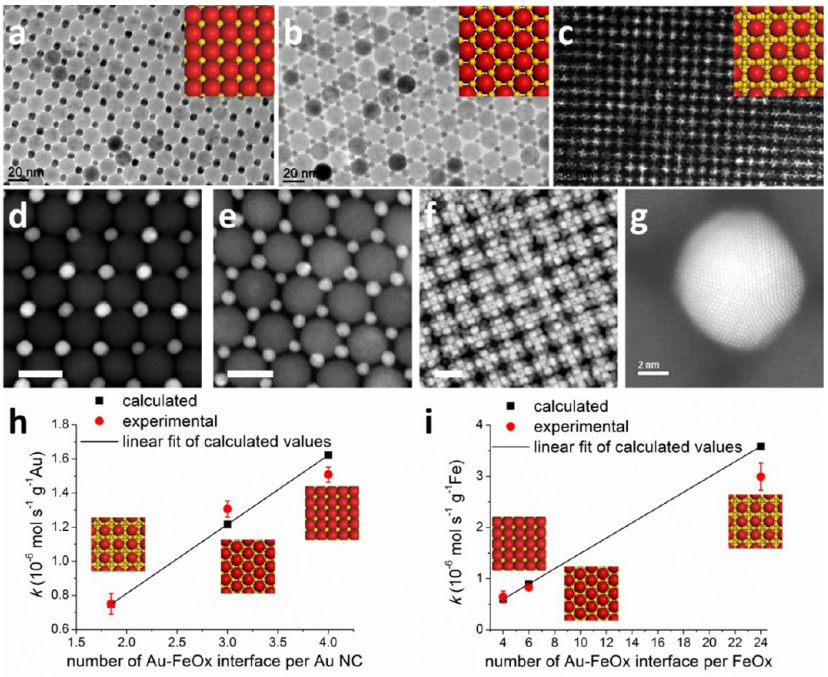

Figure 2. TEM images of (a) AB, (b) AB_2, and (c) AB_{13} Au-FeO_x BNSLs; STEM-HAADF images of pretreated (d) AB, (e) AB_2, and (f) AB_{13} Au-FeO_x BNSLs; (g) STEM-HAADF image of AB Au-FeO_x BNSL showing one Au NC is in contact with four adjacent FeO_x NCs; the activity (reaction rate of CO oxidation expressed by the rate of CO_2 production) normalized to the mass of (h) Au and (i) Fe is a function of the number of the Au-FeO_x contacts (h) per Au NC and (i) per FeO_x NC. Scale bars: (a, b, d, f) 20 nm, (c) 50 nm, (e) 10 nm, (g) 2 nm.

samples loaded on silicon monoxide films covered TEM grids are also employed to check the stability after the pretreatment (in pure O_2, 180 °C, 30 min), and catalytic property measurements.

RESULTS AND DISCUSSION

According to the widely accepted Langmuir−Hinshelwood mechanism, both CO and O_2 need to adsorb on catalyst surface to facilitate CO oxidation. The rate limiting step is the adsorption and dissociation of O_2.[36] However, the adsorption strength of O_2 molecules on a Au surface is negligibly weak at typical conditions used in practical CO oxidation.[36−39] Thus, bulk Au had long been considered to be catalytically inactive toward CO oxidation. However, some Au catalysts supported on oxides, especially on iron oxides, have been identified to be extremely active for CO oxidation, even at ambient temperature.[40−43] The origin of such high activity is currently under debate.[37,38,41,43−47] One common argument is that only small Au particles below a critical size are active.[41,43,46] The critical size is reported in the range of 0.5−5 nm, with Au particles larger than 5 nm generally regarded to be inactive for low-temperature CO oxidation. However, Sun, et al. have synthesized Au−Fe_3O_4 dumbbell nanoparticles (heterodimers) composed of 5 nm Au attached to 12 nm Fe_3O_4 and have found them to be active toward CO oxidation, even below 0 °C.[48]

We observe active CO oxidation on random mixture of 6 nm Au NCs and 16 nm Fe_3O_4 NCs (Figure S1), while pure 16 nm Fe_3O_4 NCs exhibits little activity and pure 6 nm Au is inactive for CO oxidation under the same reaction condition. These two results suggest that Au may not necessarily need to be smaller than 5 nm to be active in Au-FeO_x catalysts: instead this implies that the interaction between Au and FeO_x is responsible for the exceptional activity. We take advantage of the structural control available in BNSLs to confirm experimentally that the active sites correspond to the interparticle contacts. BNSLs offer two major advantages. First, the size of building blocks can be precisely controlled, eliminating any uncertainties arising from polydispersity of the catalyst or support. In this study, we maintain the size of Au NCs at 6 nm, to ensure the individual Au NC will not contribute significantly to the overall activity unless it is in contact with FeO_x (because Au NCs themselves are inactive if their size is larger than 5 nm). Second, the structure of BNSLs is tunable, allowing us to adjust stoichiometry of Au:Fe and to rigorously control the number of contacts between Au and FeO_x NCs.

Among the available structures, we choose AB, AB_2, and AB_{13} as they can be produced in high phase-purity with coherently packed domains (grains) on the order of μm^2 forming continuous films covering areas on the order of cm^2. In the AB structure (Figure 2a), each Au NC makes contact with 4 neighboring FeO_x NCs, and vice versa. For AB_2 monolayer BNSL (Figure 2b), the number of contacts is 6 per FeO_x NC and 3 per Au NC, while the AB_{13} structure (Figure 2c) exhibits 24 contacts per FeO_x and 2 per Au. The effective contact number per Au for AB_{13} is 1.85 (2 × 12/13), because the Au NCs are arranged in an icosahedron, where 12 Au NCs are on the exterior and the 13th resides in the interior with no contact to FeO_x.

The BNSLs are made through self-assembly at a liquid−air interface,[22] and then are transferred onto Si wafers and loaded into a batch reactor for catalytic studies. The overall reaction rate is proportional to the loading of catalysts, indicating that the diffusion of gas molecules is not rate limiting. In addition, we mathematically deduce a data processing method which enables the determination of reaction rate with each data point while minimizing a common source of error that is from the uncertainty in the sampling volume (dose) for the injection-mode GC measurements (see Supporting Information). The reaction temperature is chosen to be 150 °C: this relatively high

dx.doi.org/10.1021/ja310427u | J. Am. Chem. Soc. 2013, 135, 1499−1505

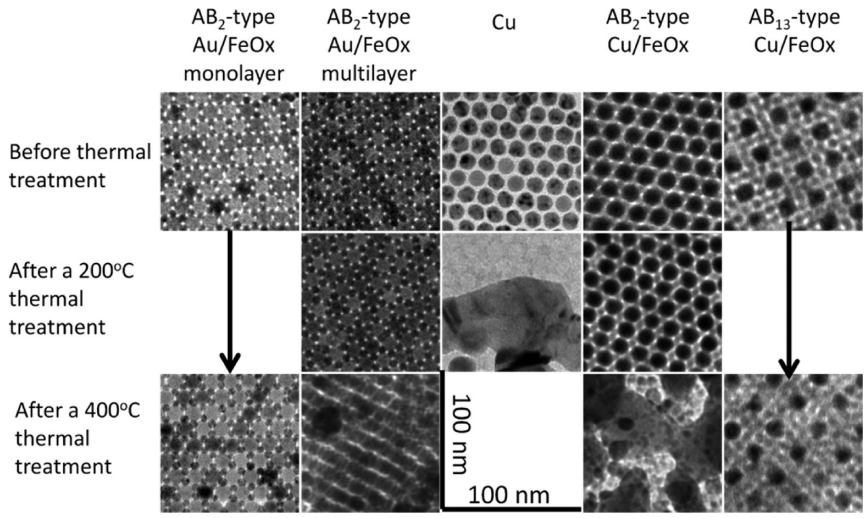

Figure 3. Structure-dependent thermal stability of NCs and NC superlattice. All TEM images are 100 nm × 100 nm.

temperature is chosen so as to obtain higher reaction rates to compensate for the low catalyst loading. This ensures that the concentration of CO_2 is sufficiently high to be detected by GC, yet this is a sufficiently low temperature that the activity of individual Au or FeO_x is negligible. In addition, the morphology of the BNSL catalysts does not change at 150 °C (Figure S18). The high-angle annular dark-field scanning transmission electron microscopy (HAADF-STEM) images shown in Figure 2d–f represent the BNSL catalysts (pretreated, see Methods). The Au NC makes direct contact with neighboring FeO_x NCs after the removal of organic stabilizers, as is evident the atomic resolution HAADF-STEM image in Figure 2g.

With the size of building blocks fixed, we assume the area and the perimeter of each contact between Au and FeO_x are also constant. Therefore, according to our hypothesis that the active site is the contact, we predict that the overall activity should be proportional to the number of catalytic contacts. And, in fact, our measurements on Au-FeO_x BNSLs directly support this hypothesis, as shown in Figure 2h,i. The overall specific rates are normalized to the mass of Au or Fe, respectively, and then plotted versus the number of Au-FeO_x contacts in the structure. Because the AB_2 BNSL has the largest domain size, the rates obtained on AB_2 Au-FeO_x are averaged to provide a relative rate per Au-FeO_x contact and then this reference is used to predict expected activity of AB and AB_{13} based on their respective number of Au-FeO_x contacts. The experimental rates of CO oxidation on AB and AB_{13} are consistent with the linear correlation from the rate per contact calculated for the AB_2 structure. Given that the Au and FeO_x show negligible activity at same reaction conditions, this linear correlation between the overall activities and the density of Au-FeO_x contacts is strong evidence that the contacts of Au-FeO_x are the active sites for CO oxidation. Moreover, changing the size of FeO_x NCs in the BNSLs changes the activity per FeO_x NC but does not significantly change the activity per Au NC (Table S3), thus providing further confirmation of the hypothesis. On another hand, as shown in Table S2 and Figure S3, disordered mixtures of Au and FeO_x NCs show significantly lower activities (except mixture 5) compared to the ordered BNSLs. This can be ascribed to the reduced density of Au-FeO_x contacts due to local phase-segregation. Although mixture 5 lacks intermediate and long-range order, the composition (confirmed by ICP-OES) and size ratio of the constituents approach the optimum packing for AB_5 BNSL (equivalent to the atomic $CaCu_5$ crystal structure). This suppresses phase separation and provides a high density of Au-FeO_x contacts (Figure S3) which in turn results in a high reaction rate per FeO_x particle. When same Au and FeO_x NCs are loaded onto opposite sides of a Si Wafer (i.e., when no Au-FeO_x contact exists) and tested in equivalent conditions, the sample shows negligible activity toward CO oxidation. This again strongly suggests that the Au-FeO_x interaction at the contacts is necessary for the observed catalytic activity.

As described earlier, the low activity on pure Au is ascribed to the weak adsorption of O_2 on Au. Our density functional theory (DFT) study of the adsorption at the contact between Au and FeO_x surfaces indicates that the adsorption of O_2 is strongest at the contact where the energy for adsorption (E_{ads}) is −0.73 eV, and the adsorption strength drops quickly as the adsorption site moves away from the Au-FeO_x contact (Figure S4). While CO adsorbs on Au surface,[49] the enhanced adsorption strength of O_2 is essential to facilitate the CO oxidation by lowering its reaction barrier.[39] Additionally, as O_2 can adsorb and dissociate on FeO_x, at the temperature of reaction the migration of O to Au or Au-FeO_x interface may occur to promote CO oxidation. Many possible mechanisms for the CO oxidation at Au-oxide interface have been discussed.[49−55] Nevertheless, in addition to many works studying the effect of the Au−oxide interface that eliminate Au particle size effects,[9,18,52−54,56] our results provide direct evidence that instead of the small Au particles, the Au-FeO_x contact is responsible for the high activity.

The overall activities obtained on BNSLs are about 2 orders of magnitude lower than the reported best current catalysts. However, the turnover frequency (TOF) normalized to total number of contacts is close to 1 s^{-1}, which is the same order of magnitude as reported high TOFs.[43] This can be explained by the actual number of active sites. Assuming the NCs are nearly spherical, the atoms involved in the contact are described in Figure S11. For 6 nm Au NCs, the individual atoms at the Au-FeO_x contact represent only 0.48% of the total Au loading. However, the number for 0.5 nm Au cluster is 50%, which means for the same Au loading the 0.5 nm Au NCs possess approximately 100 times more "active" Au atoms than a 6 nm Au NCs. This suggests that the number of active sites at the Au-FeO_x contact can be increased by decreasing the Au NC size. Our results thus indicate that it is not so much that small sizes

dx.doi.org/10.1021/ja310427u | J. Am. Chem. Soc. 2013, 135, 1499−1505

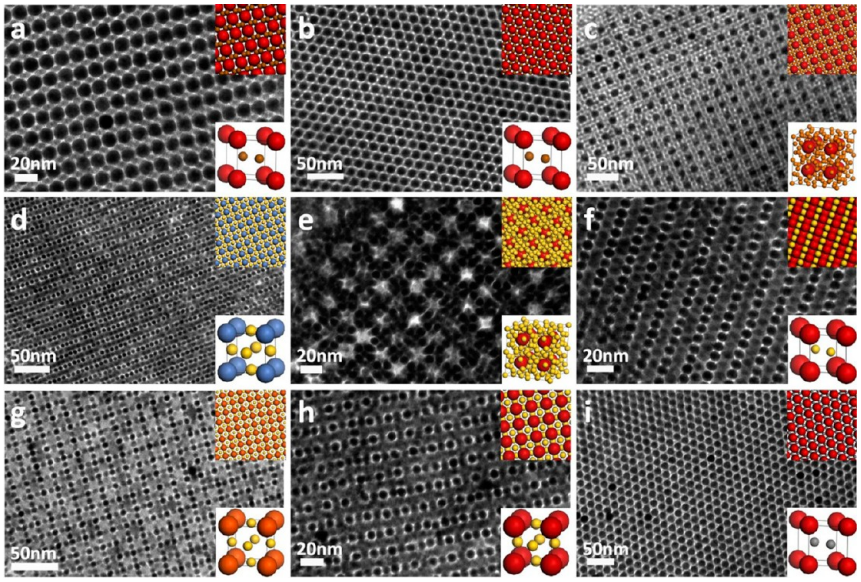

Figure 4. A selection of available BNSLs. (a and b) AB_2 Cu-FeO_x, (c) AB_{13} Cu-FeO_x, (d) AB_3 Au-Ni, (e) AB_{13} Cu-Au, (f) AB_2 Cu-Au, (g) AB_3 Au-FeO_x, (h) AB_3 Cu-Au, (i) AB_2 Cu-MnO. The insets are cartoon structures and unit cells. Scale bars: (a, e, f, h) 20 nm, (b, c, d, g, i) 50 nm.

are required for Au particle to be active in catalysis, but rather that it is desirable to maximize the number of active sites (i.e., the Au-FeO_x contact) to obtain high activity.

In addition to enabling the engineering of catalytic activity, BNSLs also hold the potential to improve the stability of catalysts. Metals usually exhibit significantly reduced melting points when their size drops into the nanometer regime – a phenomenon known as the melting-point-depression.[57] As an example, Au NCs that are 2.5 nm in diameter have been found to have their melting point reduced to around 300 °C.[57] Furthermore, the metal NCs sinter well below their reduced melting point, because of elevated mass transfer at surface. In an all metal NC system, it is very common that one particle is in contact with the other one, forming a neck (Figure S12). The large change in curvature over distance at the neck creates a capillary stress, which acts as a driving force to move the metal atoms for sintering (see Supporting Information). In addition, it is possible that a liquid phase is also involved in the sintering process, providing another important source of sintering stress.[58−60] As a demonstration of sintering at low temperature, we observe that 6 nm Au and 12 nm Cu NCs start to sinter under thermal treatment at 200 °C (in N_2). This behavior of metal sintering at relatively low temperature causes the problem of losing effective surface area of metal catalysts in the catalytic reactions, which in turn leads to a decrease in their overall activities. However, in our catalytic studies involving BNSLs, we observe that oxide-supported metals, particularly metal-oxide BNSLs with ordered structures, exhibit significantly enhanced stability at elevated temperature. Our observations are presented in Figure 3. Au-FeO_x AB_2 BNSLs retain their long-range ordered structures under a thermal treatment at 200 °C (in N_2). In contrast, the single component thin film of Au NCs and the disordered Au-FeO_x mixtures are severely sintered. As a direct demonstration, we show a thin film in Figure S13, in which the ordered and disordered domains coexist. After a 200 °C thermal treatment (in N_2), the disordered domains are sintered while the ordered domains are preserved. When the temperature of thermal treatment is further increased to 400 °C (in N_2), in an AB_2 Au-FeO_x BNSL with multilayers, Au NC sinters in the interstices formed by the lattice of larger FeO_x NCs, but the FeO_x skeleton is preserved (Figure 3 and Figure S14). In contrast, a monolayer of AB or AB_2 structure of Au-FeO_x shows little morphological change. This enhanced stability is not limited to Au-containing BNSLs. As seen in the case of Cu-FeO_x, the AB_2 (here, Cu is A, FeO_x is B) survives at 200 °C, but sinters at 400 °C. However, the AB_{13} Cu-FeO_x is stable up to 400 °C, which is a sufficient operating temperature for most industrially important catalytic reactions. These results indicate that the stability of a catalyst can be substantially improved for certain structures of BNSLs if the metal NCs are well isolated from each other, by a more thermally stable oxide. At high temperature, the adjacent Au NCs tend to coalesce if two Au particles are nearest neighbors (Figure S15). In multilayers of AB_2 Au-FeO_x, a Au NC shares interstices (from packing of FeO_x) with neighboring Au NCs in both lateral and vertical directions, while Au NCs in the monolayer are isolated by FeO_x NCs in one plane. This causes an increased probability of coalescence in a multilayer compared to a monolayer. Moreover, as described earlier, the wetting liquid (from melted Au) may increase the probability of coalescence to form a neck, and therefore facilitates the sintering process. However, in the AB_2 structure, especially in monolayer AB_2, the large sized FeO_x NCs appear to block mass transfer between the Au NCs and the wetting of liquid Au, alleviating the sintering. In AB_2 Cu-FeO_x, Cu is the larger of the two building blocks, and thus, the distance between two Cu NCs is insufficient to prevent coalescence. Specifically, the liquid Cu can spread over the surface (wetting) and thereby provide an easy mass-transport route between Cu NCs (Figure S16). In contrast, in an AB_{13} Cu-FeO_x BNSL, the metal NCs are well-separated spatially and thus they do not coalesce. By using BNSLs as models, we demonstrate a general strategy of keeping metal NCs precisely separated to enhance the stability of metal catalysts, consistent with recent reports.[25,61] Our recent result shows that in FePt-MnO the well-confined FePt can be stable up to 650 °C.[25]

Moreover, we have a great diversity of available compositions and structures of BNSLs, including such catalytically relevant combinations as Pt-Pd, Pt-Au, Pt-Ni, Pt-MnO, Pt-FeO_x, FePt-FeO_x, $CoPt_3$-FeO_x, FePt-MnO, Au-Cu, Ni-Cu, Au-Ni, Au-

dx.doi.org/10.1021/ja310427u | J. Am. Chem. Soc. 2013, 135, 1499−1505

FeO_x, Cu-FeO_x, Pd-FeO_x, and MnO-FeO_x all in a variety of crystal structures.[22,25,29] A demonstration of the range of BNSLs is presented in Figure 4. These BNSLs can be used as models to study other catalytic reactions as demonstrated in the case of Au-FeOx. For instance, Pt−Ni and Au−Ni can be used to study methanol reforming reaction and the Pd-FeO_x can be used to understand the catalytic process of water gas shift reaction.

CONCLUSION

In summary, we identify the active sites for a Au-FeO_x catalyst by using Au-FeO_x BNSLs in well-defined structures. We also exploit the BNSL architecture to enhance the thermal stability of catalysts, by suppressing sintering and coalescence. Thus, we establish that NC superlattices are useful model materials through which to explore, understand, and improve catalytic processes. As the variety of available building blocks increases, it is expected that NC superlattices will provide a powerful new platform for research in the field of catalysis that bridges traditional studies of single crystals and supported particulate catalysts.

ASSOCIATED CONTENT

Supporting Information

More experimental details of CO oxidation on Au-FeO_x BNSLs, details of DFT calculations, discussion of sintering, additional TEM, HAADF-STEM, AFM images and EDX maps. This material is available free of charge via the Internet at http://pubs.acs.org.

AUTHOR INFORMATION

Corresponding Author

cbmurray@sas.upenn.edu

Notes

The authors declare no competing financial interest.

ACKNOWLEDGMENTS

C.B.M. and Y.K. acknowledge the partial support from the National Science Foundation MRSEC DMR11-20901, and the U.S. Army Research Office (ARO) under Award MURI W911NF-08-1-0364. X.Y. acknowledges the support from the Office of Naval Research (ONR) Multidisciplinary University Research Initiative (MURI) on Optical Metamaterials through award N00014-10-1-0942. J.C. and V.D.-N. acknowledge the DOE Office of ARPA-E for support under Award DE-AR0000123. G.X. and C.R.K. acknowledge support from the U.S. Department of Energy, Office of Basic Energy Sciences, Division of Materials Science and Engineering, under Award No. DE-SC0002158. L.Q. and J.L. acknowledge support by NSF DMR-1120901 and AFOSR FA9550-08-1-0325. C.B.M. thanks the Richard Perry University Professorship for the support of his supervisor role. Research carried out in part at the Center for Functional Nanomaterials (CFN), Brookhaven National Laboratory (BNL), which is supported by the U.S. Department of Energy, Office of Basic Energy Sciences, under Contract No. DE-AC02-98CH10886. We thank Naoki Kikuchi from JEOL for the extraordinary SEM image (Figure 1a), Charles Black and Fernando Camino (CFN, BNL) for the support at CFN, and David Vann at Department of Earth and Environmental Science (University of Pennsylvania) for assistance in ICP-OES.

REFERENCES

(1) Mizuno, N.; Misono, M. *Chem. Rev.* **1998**, *98*, 199−217.
(2) Somorjai, G. A. *Chem. Rev.* **1996**, *96*, 1223−1235.
(3) Gunter, P. L. J.; Niemantsverdriet, J. W.; Ribeiro, F. H.; Somorjai, G. A. *Catal. Rev. Sci. Eng.* **1997**, *39*, 77−168.
(4) Li, Y.; Somorjai, G. A. *Nano Lett.* **2010**, *10*, 2289−2295.
(5) Lee, I.; Delbecq, F.; Morales, R.; Albiter, M. A.; Zaera, F. *Nat. Mater.* **2009**, *8*, 132−138.
(6) Narayanan, R.; El-Sayed, M. A. *Nano Lett.* **2004**, *4*, 1343−1348.
(7) Bratlie, K. M.; Lee, H.; Komvopoulos, K.; Yang, P. D.; Somorjai, G. A. *Nano Lett.* **2007**, *7*, 3097−3101.
(8) Habas, S. E.; Lee, H.; Radmilovic, V.; Somorjai, G. A.; Yang, P. D. *Nat. Mater.* **2007**, *6*, 692−697.
(9) Fu, Q.; Saltsburg, H.; Flytzani-Stephanopoulos, M. *Science* **2003**, *301*, 935−938.
(10) Si, R.; Flytzani-Stephanopoulos, M. *Angew. Chem., Int. Ed.* **2008**, *47*, 2884−2887.
(11) Buck, M. R.; Bondi, J. F.; Schaak, R. E. *Nat. Chem.* **2012**, *4*, 37−44.
(12) Kang, Y. J.; Murray, C. B. *J. Am. Chem. Soc.* **2010**, *132*, 7568−7569.
(13) Kang, Y. J.; Qi, L.; Li, M.; Diaz, R. E.; Su, D.; Adzic, R. R.; Stach, E.; Li, J.; Murray, C. B. *ACS Nano* **2012**, *6*, 2818−2825.
(14) Kang, Y. J.; Pyo, J. B.; Ye, X. C.; Gordon, T. R.; Murray, C. B. *ACS Nano* **2012**, *6*, 5642−5647.
(15) Wang, C.; Chi, M.; Li, D.; Strmcnik, D.; van der Vliett, D.; Wang, G.; Komanicky, V.; Chang, K.-C.; Paulikas, A. P.; Tripkovic, D.; Pearson, J.; More, K. L.; Markovic, N. M.; Stamenkovic, V. R. *J. Am. Chem. Soc.* **2011**, *133*, 14396−14403.
(16) Wang, C.; van der Vliet, D.; More, K. L.; Zaluzec, N. J.; Peng, S.; Sun, S. H.; Daimon, H.; Wang, G. F.; Greeley, J.; Pearson, J.; Paulikas, A. P.; Karapetrov, G.; Strmcnik, D.; Markovic, N. M.; Stamenkovic, V. R. *Nano Lett.* **2011**, *11*, 919−926.
(17) Zuburtikudis, I.; Saltsburg, H. *Science* **1992**, *258*, 1337−1339.
(18) Zhou, Z.; Kooi, S.; Flytzani-Stephanopoulos, M.; Saltsburg, H. *Adv. Funct. Mater.* **2008**, *18*, 2801−2807.
(19) Jacobs, P. W.; Ribeiro, F. H.; Somorjai, G. A.; Wind, S. J. *Catal. Lett.* **1996**, *37*, 131−136.
(20) Grunes, J.; Zhu, J.; Anderson, E. A.; Somorjai, G. A. *J. Phys. Chem. B* **2002**, *106*, 11463−11468.
(21) Yamada, Y.; Tsung, C. K.; Huang, W.; Huo, Z. Y.; Habas, S. E.; Soejima, T.; Aliaga, C. E.; Somorjai, G. A.; Yang, P. D. *Nat. Chem.* **2011**, *3*, 372−376.
(22) Dong, A. G.; Chen, J.; Vora, P. M.; Kikkawa, J. M.; Murray, C. B. *Nature* **2010**, *466*, 474−477.
(23) Shevchenko, E. V.; Talapin, D. V.; Kotov, N. A.; O'Brien, S.; Murray, C. B. *Nature* **2006**, *439*, 55−59.
(24) Chen, J.; Dong, A. G.; Cai, J.; Ye, X. C.; Kang, Y. J.; Kikkawa, J. M.; Murray, C. B. *Nano Lett.* **2010**, *10*, 5103−5108.
(25) Dong, A. G.; Chen, J.; Ye, X. C.; Kikkawa, J. M.; Murray, C. B. *J. Am. Chem. Soc.* **2011**, *133*, 13296−13299.
(26) Korgel, B. A. *Nat. Mater.* **2007**, *6*, 551−552.
(27) Smith, D. K.; Goodfellow, B.; Smilgies, D. M.; Korgel, B. A. *J. Am. Chem. Soc.* **2009**, *131*, 3281−3290.
(28) Friedrich, H.; Gommes, C. J.; Overgaag, K.; Meeldijk, J. D.; Evers, W. H.; de Nijs, B.; Boneschanscher, M. P.; de Jongh, P. E.; Verkleij, A. J.; de Jong, K. P.; van Blaaderen, A.; Vanmaekelbergh, D. *Nano Lett.* **2009**, *9*, 2719−2724.
(29) Dong, A. G.; Ye, X. C.; Chen, J.; Murray, C. B. *Nano Lett.* **2011**, *11*, 1804−1809.
(30) Ye, X. C.; Chen, J.; Murray, C. B. *J. Am. Chem. Soc.* **2011**, *133*, 2613−2620.
(31) Sun, S. H.; Murray, C. B.; Weller, D.; Folks, L.; Moser, A. *Science* **2000**, *287*, 1989−1992.
(32) Murray, C. B.; Sun, S. H.; Doyle, H.; Betley, T. *MRS Bull.* **2001**, *26*, 985−991.
(33) Kang, Y. J.; Ye, X. C.; Murray, C. B. *Angew. Chem., Int. Ed.* **2010**, *49*, 6156−6159.

(34) Park, J.; An, K. J.; Hwang, Y. S.; Park, J. G.; Noh, H. J.; Kim, J. Y.; Park, J. H.; Hwang, N. M.; Hyeon, T. *Nat. Mater.* **2004**, *3*, 891−895.
(35) Hung, L. I.; Tsung, C. K.; Huang, W. Y.; Yang, P. D. *Adv. Mater.* **2010**, *22*, 1910−1914.
(36) Deng, X. Y.; Min, B. K.; Guloy, A.; Friend, C. M. *J. Am. Chem. Soc.* **2005**, *127*, 9267−9270.
(37) Min, B. K.; Alemozafar, A. R.; Pinnaduwage, D.; Deng, X.; Friend, C. M. *J. Phys. Chem. B* **2006**, *110*, 19833−19838.
(38) Meyer, R.; Lemire, C.; Shaikhutdinov, S. K.; Freund, H. *Gold Bull.* **2004**, *37*, 72−124.
(39) Lopez, N.; Norskov, J. K. *J. Am. Chem. Soc.* **2002**, *124*, 11262−11263.
(40) Haruta, M.; Date, M. *Appl. Catal., A* **2001**, *222*, 427−437.
(41) Haruta, M. *Catal. Today* **1997**, *36*, 153−166.
(42) Haruta, M.; Tsubota, S.; Kobayashi, T.; Kageyama, H.; Genet, M. J.; Delmon, B. *J. Catal.* **1993**, *144*, 175−192.
(43) Herzing, A. A.; Kiely, C. J.; Carley, A. F.; Landon, P.; Hutchings, G. J. *Science* **2008**, *321*, 1331−1335.
(44) Lopez, N.; Janssens, T. V. W.; Clausen, B. S.; Xu, Y.; Mavrikakis, M.; Bligaard, T.; Norskov, J. K. *J. Catal.* **2004**, *223*, 232−235.
(45) Hashmi, A. S. K.; Hutchings, G. J. *Angew. Chem., Int. Ed.* **2006**, *45*, 7896−7936.
(46) Liu, Y.; Jia, C. J.; Yamasaki, J.; Terasaki, O.; Schuth, F. *Angew. Chem., Int. Ed.* **2010**, *49*, 5771−5775.
(47) Min, B. K.; Friend, C. M. *Chem. Rev.* **2007**, *107*, 2709−2724.
(48) Wang, C.; Yin, H. F.; Dai, S.; Sun, S. H. *Chem. Mater.* **2010**, *22*, 3277−3282.
(49) Chen, M. S.; Goodman, D. W. *Science* **2004**, *306*, 252−255.
(50) Remediakis, I. N.; Lopez, N.; Norskov, J. K. *Angew. Chem., Int. Ed.* **2005**, *44*, 1824−1826.
(51) Schubert, M. M.; Hackenberg, S.; van Veen, A. C.; Muhler, M.; Plzak, V.; Behm, R. J. *J. Catal.* **2001**, *197*, 113−122.
(52) Rodriguez, J. A.; Ma, S.; Liu, P.; Hrbek, J.; Evans, J.; Perez, M. *Science* **2007**, *318*, 1757−1760.
(53) Yan, T.; Redman, D. W.; Yu, W.-Y.; Flaherty, D. W.; Rodriguez, J. A.; Mullins, C. B. *J. Catal.* **2012**, *294*, 216−222.
(54) Park, J. B.; Graciani, J.; Evans, J.; Stacchiola, D.; Ma, S.; Liu, P.; Nambu, A.; Fernandez Sanz, J.; Hrbek, J.; Rodriguez, J. A. *Proc. Natl. Acad. Sci. U.S.A.* **2009**, *106*, 4975−4980.
(55) Green, I. X.; Tang, W.; Neurock, M.; Yates, J. T., Jr. *Science* **2011**, *333*, 736−739.
(56) Zhou, Z.; Flytzani-Stephanopoulos, M.; Saltsburg, H. *J. Catal.* **2011**, *280*, 255−263.
(57) Buffat, P.; Borel, J. P. *Phys. Rev. A* **1976**, *13*, 2287−2298.
(58) Couchman, P. R.; Jesser, W. A. *Nature* **1977**, *269*, 481−483.
(59) Frenken, J. W. M.; Vanderveen, J. F. *Phys. Rev. Lett.* **1985**, *54*, 134−137.
(60) Sakai, H. *Surf. Sci.* **1996**, *351*, 285−291.
(61) Joo, S. H.; Park, J. Y.; Tsung, C.-K.; Yamada, Y.; Yang, P. D.; Somorjai, G. A. *Nat. Mater.* **2009**, *8*, 126−131.